Laser ablation characteristics of yttria-doped zirconia in the nanosecond and femtosecond regimes

S. Heiroth,[1] J. Koch,[2] T. Lippert,[1,a)] A. Wokaun,[1] D. Günther,[2] F. Garrelie,[3] and M. Guillermin[3]
[1]*Department of General Energy Research, Paul Scherrer Institut, 5232 Villigen-PSI, Switzerland*
[2]*Laboratory of Inorganic Chemistry, ETH Zurich, Wolfgang-Pauli-Strasse 10, 8093 Zurich, Switzerland*
[3]*Laboratoire Hubert Curien (UMR 5516 CNRS), Université Jean Monnet, 18 Rue Pr B. Lauras, 42000 Saint Etienne, France*

(Received 4 August 2009; accepted 22 November 2009; published online 8 January 2010)

The laser ablation characteristics of yttria-stabilized zirconia (YSZ) have been investigated as a function of the target microstructure and dopant level for different nanosecond- [ArF, KrF, and XeCl excimers; Nd:YAG (yttrium aluminum garnet) (fourth harmonic)] and femtosecond-laser sources [Ti:sapphire (fundamental and third harmonic)]. Particle ejection, which compromises the quality of coatings prepared by pulsed laser deposition (PLD), was analyzed in detail. Nanosecond-laser pulses cause a severe thermomechanical surface cracking and exfoliation of micron-sized fragments on a microsecond to millisecond time scale in the case of 8–9.5 mol % Y_2O_3-doped, fully stabilized zirconia (8YSZ and 9.5YSZ) targets. As a consequence of the intrinsic material brittleness, fully stabilized YSZ coatings deposited by PLD contained particles for all tested conditions. Lower doped partially stabilized zirconia (3YSZ) exhibits a superior fracture toughness attributed to a laser-induced partial transition to the monoclinic phase, detected by Raman spectroscopy, which enables the deposition of particle-free dense thin films by conventional PLD using nanosecond-UV laser radiation at moderate fluences of 1.2–1.5 J/cm^2. The ablation dynamics of ultrashort laser pulses differ fundamentally from the nanosecond regime as evidenced, e.g., by time-resolved shadowgraphy and light scattering experiments. Femtosecond pulses prevent the exfoliation of micron-sized fragments but result invariably in a pronounced ejection of submicron particles. The resulting PLD coatings are porous and reveal a large surface roughness as they consist of an agglomeration of nanoparticles. Femtosecond-NIR pulses provide a factor of 2.5–10 higher material removal rates compared to nanosecond- and femtosecond-UV pulses. The ablation metrics, i.e., threshold fluence and effective absorptivity, mainly depend on the laser wavelength while the pulse duration, target microstructure, and dopant level are of minor importance. Evidence is presented that incubation effects play a significant role in nanosecond- and femtosecond-laser ablations of YSZ enabling material removal at comparatively low fluences for sub-bandgap photon energies. © *2010 American Institute of Physics*. [doi:10.1063/1.3275868]

I. INTRODUCTION

Zirconia-based ceramics represent a versatile class of materials of increasing technological importance. Aliovalent dopants such as CaO, MgO, Y_2O_3, or Sc_2O_3, soluble in ZrO_2, stabilize the metastable tetragonal and cubic phases and impart oxygen ion conductivity at high temperatures. Depending on the dopant concentration and heat treatment, partially stabilized zirconia (PSZ), renowned for its outstanding mechanical properties, or fully stabilized cubic zirconia (FSZ), which is a common solid electrolyte material in high temperature electroceramic devices, can be obtained.[1,2] Additional thermal and chemical stabilities, biological compatibility, and interesting optical properties have opened a wide field of application for yttria-stabilized zirconia (YSZ) thin films as thermal barrier layers,[3] optical or antiwear coatings,[4] high-*k* dielectrics in metal-oxide-semiconductor technology,[5–7] buffer layer in superconductor thin film growth,[8] and solid electrolyte layer in miniaturized gas sensors[9] and fuel cells.[10] Most of these applications stringently require dense layers devoid of microscopic defects. This is particularly important for solid oxide fuel cell (SOFC) membranes where the gradient in the oxygen partial pressure between the anode and the cathode side, as the electrochemical driving force of the electrical power generation, has to be maintained by a gas impermeable YSZ electrolyte layer.[11]

Pulsed laser deposition (PLD) generally enables the deposition of highly dense films and has proven its efficiency in growing oxides of complex stoichiometry,[12] which is often attributed to a congruent material transfer. The feasibility of large-area PLD coatings, which is important from a technological perspective, has been demonstrated recently.[13] However, as a major drawback, the laser-target interaction frequently does not yield only atomized vapor but also condensed phase fragments. Droplets, particles, etc., are ejected and impinge on the growing film causing local damage.[14] Numerous variations of the conventional PLD

a)Author to whom correspondence should be addressed. Tel.: +41 (0)56 3104076. FAX: +41 (0)56 3102688. Electronic mail: thomas.lippert@psi.ch.

TABLE I. Laser systems and parameters employed for the ablation experiments.

Laser	λ (nm)	hν (eV)	τ_p	f (Hz)	Beam profile
Lambda Physik LPX 301i ArF excimer[a]	193	6.42	25 ns	5	Flat-top
Lambda Physik LPX 105e KrF excimer	248	5.00	20 ns	5	Flat-top
Lambda Physik COMPex 205 XeCl excimer	308	4.03	30 ns	5	Flat-top
Quantel Brilliant B Nd:YAG (4ω)	266	4.66	5 ns	10	Gaussian
BMI/TCL Concerto Ti:sapphire (1ω) [a]	795	1.56	200 fs	1000	Gaussian
Coherent Legend Ti:sapphire (1ω,3ω)	795	1.56	150 fs	5	Gaussian
	266	4.66	150 fs	5	Gaussian

[a]Used for PLD experiments.

setup have been devised to reduce the amount of particles being transferred, e.g., by an off-axis geometry,[15] shadow masks ("eclipse PLD")[16,17] in combination with a magnetic field (so-called Aurora PLD),[18] velocity filters,[19] a double laser pulse approach[20] or the use of ultrafast lasers,[21] and pulse shaping.[22] Despite the remarkable achievements these techniques reveal different shortcomings such as diminished deposition rates, a nonuniform film growth, their technical complexity, or material dependent applicability. It is therefore highly desirable to optimize the conventional PLD process. Knowledge about the characteristics of the target material in the laser ablation step provides the key to an optimization of the laser parameters and target properties to achieve an elimination of particle ejection. Up to now, the few studies on the laser ablation characteristics of zirconia-based ceramics focus mainly on microstructuring aspects[23,24] or plasma diagnostics[25–27] and remain predominantly restricted to a single type of target, respectively laser source.

The present work aims at a comprehensive investigation of the ablation characteristics of YSZ with a particular emphasis on particle ejection to evaluate ablation conditions enabling the growth of particle-free YSZ films by conventional PLD. YSZ targets of different microstructures and dopant levels, as well as different laser sources with short, respectively, ultrashort pulses covering photon energies ranging across the optical bandgap of the material, are investigated.

II. EXPERIMENTAL

Table I provides an overview of the different laser sources employed for ablation experiments in air covering a photon energy range from well below to above the bandgap energy of zirconia (5.5–5.8 eV). The chirped pulsed amplification type Ti:sapphire system and its optical setup for harmonics generation are described in detail elsewhere.[28] The pulse duration was derived from the spectral full width at half maximum of the fundamental radiation, assuming the pulse to be Fourier limited.

The following targets were chosen to study the effects of dopant level, i.e., the crystallographic phase composition, and microstructure, on the ablation characteristics.

(a) Polycrystalline pellets obtained by uniaxial pressing of 8 mol % (8YSZ, fully stabilized), respectively, 3 mol % Y_2O_3-doped ZrO_2 (3YSZ, partially stabilized) powder (Tosoh Corp.) at 4.0 kbars and subsequent sintering for 10 h at 1600 °C. The microcrystalline sintered pellets were ground using a SiC abrasive paper and polished to a mirror finish with diamond suspensions yielding a rms surface roughness of 5.0 ± 0.7 nm, respectively, 6.8 ± 0.6 nm.

(b) (100) oriented single crystals of 9.5 mol % Y_2O_3-doped ZrO_2 (9.5YSZ, fully stabilized, Crystec) with a rms surface roughness <0.4 nm.

Nanosecond-laser ablation experiments were performed using an imaging setup. A square aperture cutting a central homogeneous part of the laser beam was projected by an UV-grade fused silica lens (f: +100 mm) onto the surface of the ceramic target, which was mounted on an XYZ stage, to yield a spot size of $\sim 250 \times 250$ μm^2. In the case of the femtosecond pulses, the full beam was projected onto the target surface by an UV-grade quartz lens (f: +50 mm) while the sample was positioned above the focal plane to avoid a breakdown in air and to regulate the spot size to a diameter of ~ 175 μm for femtosecond-NIR pulses, respectively, ~ 55 μm for femtosecond-UV pulses. The pulse energy measured with a pyroelectric detector was adjusted by a variable dielectric attenuator for the nanosecond pulses, respectively, a set of gray filters for the femtosecond pulses to yield fluences in the range of 0.35 to a maximum of ~ 18 J/cm^2. The surface topography and morphology of the laser irradiated sites were analyzed as a function of the fluence and number of pulses (single pulse to 10.000) using a stylus profilometer (Dektak 8, Veeco Instruments Inc.), respectively, a field emission scanning electron microscope (FESEM) (Supra VP55, Zeiss) in variable pressure mode to avoid specimen charging. An ablation depth averaged over the spot size area was calculated based on two perpendicular central profilometric cross sections for each ablation cavity assuming ideal cuboid (nanosecond pulses), respectively, rotation symmetric (femtosecond pulses) geometry. A Raman microscope (Labram Series, Horiba Jobin Yvon) using a focused He–Ne laser (λ: 632.8 nm) source with a power of 10 mW was employed to investigate possible changes in the target crystallographic phase composition upon pulsed laser irradiation, analyzing a sample volume of ~ 1 μm^3.

Time-resolved imaging of the ablation products in air was performed using an ArF excimer (spot size on target adjusted to 150×150 μm^2) as well as femtosecond-NIR and femtosecond-UV pulses as a pump laser. The fluorescence of a Rhodamin 6G methanol solution upon excitation by the

second harmonic of a Q-switched Nd:YAG (yttrium aluminum garnet) probe laser (τ_p: 5 ns) served as stroboscopic illumination to acquire shadowgraphs depicting instantaneous differences in the refractive index above the target surface by a synchronized charge-coupled device (CCD) camera equipped with a macro-objective.[29] The variable delay time between the two lasers was controlled by a delay generator (SRS DG 535, Stanford Research Systems). A modification to the setup, described in detail elsewhere,[30] was employed to visualize specifically the generated aerosol particles by laser-induced scattering. A vertical slit aperture was used to generate an ~0.5 mm wide sheath from the probe laser beam, which is subsequently projected above the target surface. Laser light scattered from particles, present in the interaction volume, is detected by the CCD camera positioned at a 90° angle to the propagation direction of the laser sheath yielding an instantaneous image of the particle distribution above the target surface. An interference filter placed in front of the camera objective blocks light emitted by the plasma plume. Due to the horizontal polarization of the probe beam, Rayleigh scattering is mainly suppressed, thus favoring the visualization of particles and aggregates within the Debye and Mie size range, i.e., $D > 0.05\lambda$.

The particle size distribution in the submicron range was quantified with an optical high sensitivity laser aerosol spectrometer (Particle Measuring Systems Inc.) assuming a spherical geometry of the particles. A continuous flow of air (1 L/min) was utilized to transport the laser generated aerosol from a cylindrical ablation cell[28] to a dilutor (MD-19-1i, Matter Engineering) where it was diluted to 4 vol % by mixing with Ar prior to the inlet of the spectrometer. Each measurement was acquired by integrating for 50 laser pulses at a repetition rate of 1 Hz plus 10 s, which allows a complete purging of the ablation cell volume.

YSZ thin films (thickness ~500 nm) were deposited at room temperature on *c*-cut sapphire single crystal substrates. Rotating ceramic targets of 3YSZ and 8YSZ positioned at a distance of ~40 mm to the substrate were ablated by a focused laser beam incident at an angle of 45° in an oxygen background of 0.01 mbar. The dependence of the film morphology on the applied laser parameters, i.e., ablation in a fluence range 0.8–4.0 J/cm^2 by a nanosecond ArF excimer at 10 Hz, respectively, a 1 kHz Ti:sapphire laser (compare Table I) with a pulse duration of 200 fs, measured by an autocorrelator, was investigated.

III. RESULTS AND DISCUSSION

Figure 1 presents the laser ablation rates of fully stabilized YSZ targets as derived from the averaged depth of multipulse ablation cavities for the different laser sources applied. The experimental data show a reasonable agreement with the blow-off model well known for the ablation of organic polymers and tissue by pulsed (ultra)fast lasers,[31,32] which predicts a logarithmic dependence of the ablation rate d on the fluence F according to

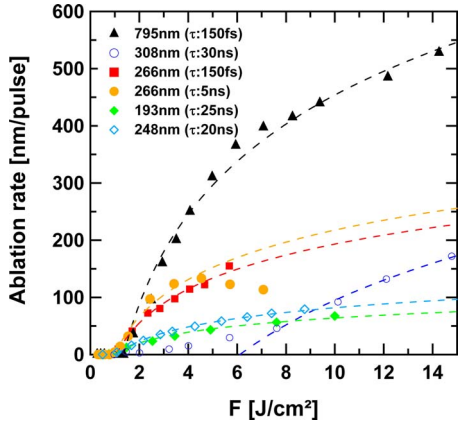

FIG. 1. (Color online) Ablation rates of fully stabilized zirconia for different laser sources [open symbols: experimental data for polycrystalline 8YSZ, closed symbols: experimental data for 9.5YSZ single crystal, and dashed lines: fit of experimental data according to Eq. (1)].

$$d = 1/\alpha_{eff} \ln(F/F_{th}). \quad (1)$$

Herein, α_{eff} represents the effective absorption coefficient and F_{th} the ablation threshold fluence.

The absolute values of the ablation rates for the UV lasers are in a range typically found for the UV laser ablation of dielectric ceramics.[23,33,34] However, the reported systematic enhancement of the material removal by ultrashort pulses cannot be confirmed in the case of YSZ. The comparison of the ablation rates obtained at a laser wavelength of 266 nm and different pulse durations shows even slightly lower rates for the femtosecond-UV pulses. Femtosecond-NIR radiation on the other hand yields up to one order of magnitude larger ablation rates compared to nanosecond pulses in the deep UV as a result of the larger penetration depth in the NIR spectral region where the target material is transparent; i.e., the energy deposition is due to multiphoton absorption. The ablation rates were derived from measurements in air; however, no fundamental changes are expected for vacuum environments.[23]

Deviations from the blow-off model can be noted in Fig. 1 for the fourth harmonic of the nanosecond-Nd:YAG above ~4 J/cm^2, where a dielectric breakdown in air occurs, and in general for all the wavelengths close to the extrapolated threshold fluence. In the case of 308 nm nanosecond radiation this latter deviation ranges from the threshold to significantly higher fluences of ~7 J/cm^2. An analogous behavior has been reported for the ablation of pure ZrO_2 by a nanosecond XeCl excimer laser.[23] This evidence could be related to a change in the ablation mechanism, e.g., from material removal by thermomechanical fragmentation to vaporization or from surface to bulk evaporation, similar to observations for polymer ablation.[31] It may alternatively be accounted for by a fluence dependence of the laser-induced persistent change in the material's absorption properties by incubation, which plays a crucial role in the laser ablation of YSZ as discussed below. The latter concept is supported by the data of Matthias *et al.*[35] showing a saturation of the change in optical absorptivity versus fluence in single pulse experiments on ZrO_2 for a photon energy below the bandgap energy. As a result of the deviations from the blow-off model at

TABLE II. Ablation threshold fluences and effective absorption coefficients as derived from linear regression of the experimental ablation rates vs ln F according to Eq. (1) and linear optical absorption coefficients from UV-vis-NIR transmission spectrum of a 500 nm thin, dense 3YSZ film on a sapphire substrate (not shown).

λ (nm)	τ_p	Target	F_{th} (J/cm^2)	α_{eff} (10^3 cm^{-1})	α_{opt} (10^3 cm^{-1})
193	25 ns	3YSZ	0.85 ± 0.10	391 ± 23	>200
		8YSZ	0.84 ± 0.10	384 ± 21	
		9.5YSZ	0.78 ± 0.11	345 ± 33	
248	20 ns	8YSZ	0.94 ± 0.09	274 ± 16	9.6
266	5 ns	3YSZ	1.09 ± 0.07	92 ± 6	1.8
		9.5YSZ	1.02 ± 0.07	97 ± 8	
	150 fs	3YSZ	1.11 ± 0.08	113 ± 8	
		9.5YSZ	1.05 ± 0.07	117 ± 6	
308	30 ns	8YSZ	1.35 ± 0.20 [a]	52 ± 6	0.13
795	150 fs	3YSZ	1.41 ± 0.15	38 ± 2	0.03
		9.5YSZ	1.44 ± 0.10	42 ± 2	

[a]Derived from a power law fit of the ablation rates at fluences ≤ 6 J/cm^2.

low fluences, the threshold values derived from linear fitting of the experimental ablation rates versus the natural logarithm of the laser fluence according to Eq. (1), which are summarized together with the effective absorption coefficients in Table II, have to be considered as an upper limit. Actual material removal has been observed at fluences that are ~15% below the thresholds listed in Table II.

The target microstructure and dopant level, as well as the pulse duration (in the UV), do not affect the ablation characteristics significantly. The ablation metrics are mainly determined by the laser wavelength as the ablation threshold increases continuously from ~0.8 to ~1.4 J/cm^2, and the effective absorption coefficient decreases from $\sim 3.8 \times 10^5$ to $\sim 4 \times 10^4$ cm^{-1} following a decreasing optical absorptivity from the deep UV ($h\nu > E_g$) to the NIR ($h\nu \ll E_g$). The standard deviation of the linear regression of the experimental data according to Eq. (1) used to derive the ablation metrics provides a measure of their uncertainty being on the order of 5%–10%. Table II reveals that the effective absorption coefficient is systematically higher than the optical absorption coefficient, far beyond the experimental error. Moreover, a visible darkening of the irradiated sites and an intensification of the material removal are detected by time-resolved imaging techniques within the first ten pulses. This suggests a formation of stable absorbing defects, i.e., in the case of YSZ, color centers.[36,37] Incubation in terms of a residual laser-induced change in the target's optical absorptivity, which accumulates over the first pulses until steady-state conditions are reached, has been demonstrated to be essential for the laser ablation process of different oxides and glasses[34,38] as well as polymers.[39] In addition to the residual modification of the optical properties, transient absorptivity changes due to absorption and scattering of the plasma plume contribute to the effective absorption.[23] Although being observed for all laser wavelengths investigated, incubation is particularly important at photon energies below the bandgap energy, i.e., corresponding to $\lambda \geq \sim 220$ nm, since it allows efficient material removal using nanosecond pulses at comparatively low fluences due to absorption by defect states occupying energy levels within the bandgap. Only the ArF excimer laser provides photons with an energy above the bandgap of YSZ, which enables an electronic photoexcitation from the valence to the conduction band by single-photon absorption. Due to the high intensities, i.e., $\sim 10^{13}$ W/cm^2, nonlinear optical absorption has to be considered in addition for ultrashort pulses. The apparent weak enhancement of α_{eff} by approximately 20% for femtosecond compared to nanosecond pulses observed at a wavelength of 266 nm (Table II) could be related accordingly to multiphoton absorption. However, the actual contribution of multiphoton absorption might be significantly larger as the probability of defect formation processes and dielectric breakdown by avalanche ionization decreases with diminishing pulse duration.[23,34] Nevertheless, the similarity of the ablation metrics at 266 nm for femtosecond and nanosecond pulses suggests a notable contribution of defect formation also for ultrashort UV pulses as previously observed for $SrTiO_3$.[33] Correspondingly, Ihlemann *et al.*[23] noted that differences in the laser pulse duration are of minor importance when the photon energy is similar to the bandgap energy allowing reasonably high single-photon absorption. In this case, neither multiphoton absorption nor plasma effects would dominate the overall ablation characteristics. Multiphoton absorption is probably more dominant for femtosecond-NIR pulses considering the optical transparency of YSZ in this spectral region. However, time-resolved imaging gives evidence that incubation still plays an important role (see Fig. 7).

The ablation rates provide exclusively information about the quantity of removed material, but no details about the physical state of this material or the underlying mechanism, which can be investigated, e.g., by time-resolved imaging techniques. Figure 2 depicts a series of shadowgraphs illustrating the temporal and spatial evolutions of the ablation

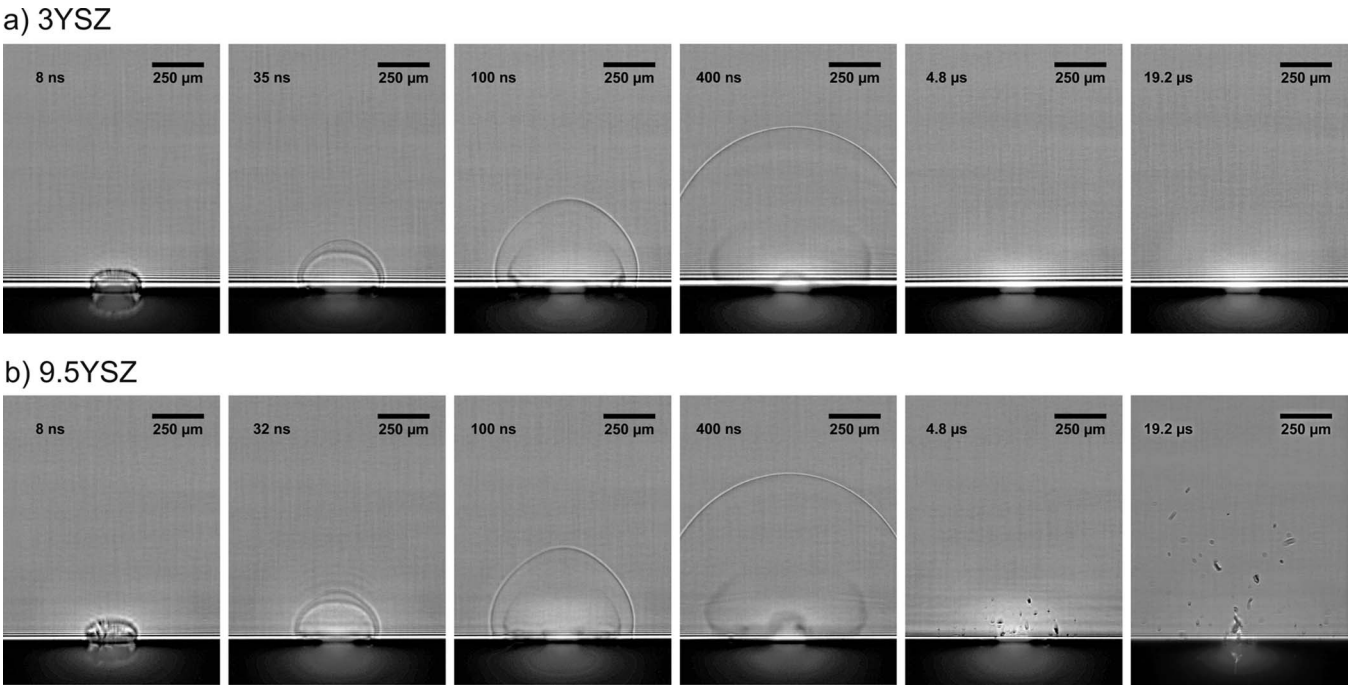

FIG. 2. Series of shadowgraphs for nanosecond-laser ablation of (a) a 3YSZ and (b) a 9.5YSZ target (λ: 193 nm, τ_p: 25 ns, 4.0 J/cm^2, and tenth pulse) recorded at different delays to the pump pulse. 8YSZ shows characteristics analogous to 9.5YSZ.

process in nanosecond-laser ablation of partially, respectively, fully stabilized zirconia. As a common feature a planar shockwave is released from the target surface practically instantaneously, i.e., during the pump pulse duration (the given delay times refer to the temporal position of the rising edges of the pump and probe laser pulse) with an initial velocity of 8–20 km/s (fluence dependent, range: 1.5–10.5 J/cm^2). The shockwave front expands subsequently compressing the surrounding air, which slows down its propagation speed to a few 100 m/s within a distance of 1 mm. During the expansion the shockwave undergoes a transition from the initial planar to a hemispherical geometry, which is due to the collisions with the surrounding gas.[40] The shockwave is followed by a second front ejected as well on a nanosecond-time scale, which attains lower initial velocities of ~3–5 km/s (fluence dependent, range: 1.5–10.5 J/cm^2). This is slowed down completely to the level of Brownian motion within 500 μm in air. As a consequence the contrast of the mushroomlike structure degrades continuously and it appears increasingly diffuse. Based on these characteristics, this second front is assigned to a vaporized material, as suggested previously.[41,42] Fully stabilized YSZ targets (8YSZ and 9YSZ) reveal an expulsion of microscopic fragments, first observed 1–2 μs after the pump laser pulse and lasting for at least 100 μs as a third characteristic feature in nanosecond ablation irrespective of the applied fluence. The velocities of the fragments with dimensions of 1–25 μm are in the range 1–100 m/s (fluence dependent, range: 1.5–10.5 J/cm^2). On the contrary, no target fragmentation is observed for partially stabilized 3YSZ targets after nanosecond-laser irradiation as Fig. 2 clearly illustrates.

Figure 3 depicts an analogous sequence of shadowgraphs for NIR femtosecond ablation of a 9.5YSZ target. Again, the release of an initial shockwave and the successive gas dynamic flow of the material vapor are observed; however, no ejection of micron-sized fragments is visible even at higher magnifications. The same behavior is detected for femtosecond-UV pulses. The shockwave reveals distortions along the optical axis upon the transition from planar to hemispherical geometry, which might be related to instabilities in the surrounding medium caused by the high power pulse. The initial velocities are about a factor of 2 lower than for nanosecond-UV pulses (λ: 193 nm) at a comparable fluence being a consequence of the lower absorptivity at the longer laser wavelength of 795 nm. Additionally the material vapor is denser and clearly visible over an extended period of time in Fig. 3 compared to Fig. 2, confirming a more efficient material removal by the ultrashort pulses in the NIR (see Fig. 1).

The shockwave propagation data of laser ablation experiments, given by the transit time t and the distance R to the origin of the explosion, may often be described efficiently with the ideal blast wave model. Applying the approach by Zeldovich and Raizer within this framework yields

$$R = \xi_0 \left(\frac{E_0}{\rho_0} \right)^{1/5} t^q \qquad (2)$$

for a strong pointlike explosion in a homogeneous medium.[43] Herein ξ_0 denotes a constant depending on the specific heat of the expanding gas, E_0 is the energy released in the explosion, ρ_0 is the undisturbed atmospheric density, and the exponent q equals 2/5 for a (hemi)spherical geometry. Figure 4 shows the fluence dependent shockwave propagation in the gas phase plotted on a double logarithmic scale for the example of a nanosecond-UV laser impact on a 9.5YSZ target.

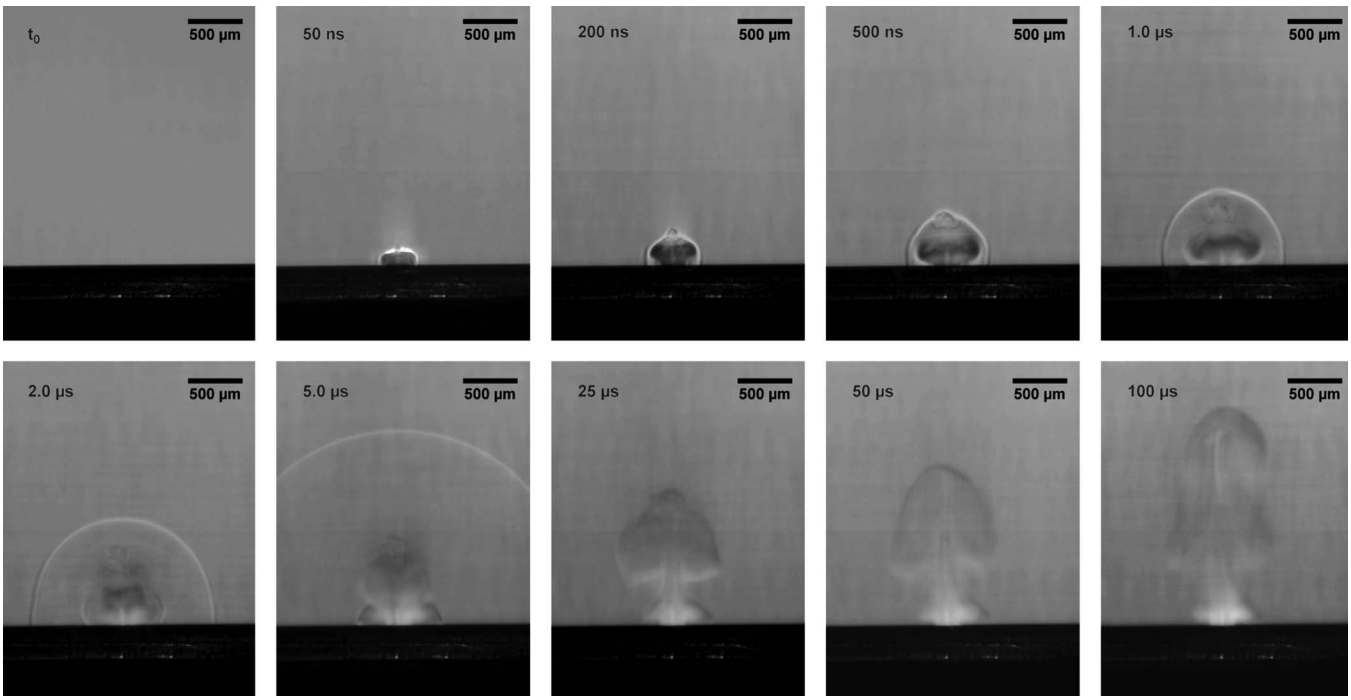

FIG. 3. Series of shadowgraphs for femtosecond-laser ablation of a 9.5YSZ target (λ: 795 nm, τ_p: 150 fs, 10.5 J/cm^2, and tenth pulse) recorded at different delay times with respect to the pump pulse.

A systematic increase in the exponent q, derived as the slope of the linear fits in the double logarithmic plot, is found for decreasing fluences. This is observed analogously for all types of investigated YSZ targets as well as for femtosecond-UV and femtosecond-NIR pulses. Values close to q=0.4, as expected from the ideal blast model, are obtained only for the highest applied fluences. The significantly larger exponents at lower fluences, attaining q-values of up to 0.65, could be caused by a change in the shape of the shockwave, but the shadowgraphs provide no evidence for a fluence dependent deviation from the hemispherical expansion geometry. It has been shown that substantial deviations from the ideal blast wave model are expected when the laser parameters do not match the model's fundamental preconditions such as a sufficient energy deposited to cause a strong shock.[42] The presented data on YSZ suggest, however, that a description of the laser generated shockwave propagation by the blast wave model is possible on a nanosecond- to microsecond-time scale for a wide range of ablation conditions if the exponent q is treated as a variable.

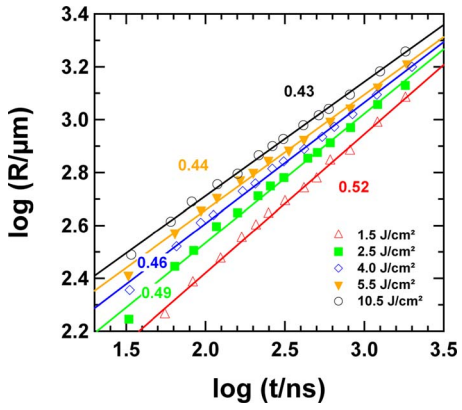

FIG. 4. (Color online) Propagation of the shockwave generated in the gas phase by pulsed nanosecond-laser impact (λ: 193 nm and τ_p: 25 ns) on a 9.5YSZ target in a double logarithmic representation for different fluences. The exponents q derived as the slope of the least squares linear fits (solid lines) according to Eq. (2) are included.

An adequate contrast for the visualization of particles is obtained in shadowgraphy only for large particles (micron range) or a sufficiently dense packaging of smaller ones. Light scattering can be used as a complementary technique to visualize, in particular, submicron particles. No micron-sized fragments could be detected by shadowgraphy for femtosecond ablation of YSZ (Fig. 3). The light scattering images in Fig. 5, however, indicate a strong directional ejection of smaller, i.e., submicron, particles. The process starts shortly after the laser pulse and lasts up to several 10 μs.

The comparison of the aerosol particle size distributions normalized to the laser spot size area A and the bin width dR (Fig. 6), i.e., the finite size range covered by an individual spectrometer channel, confirms that strong submicron particle formation is an exclusive characteristic to the ablation of YSZ with ultrashort laser pulses. This is observed for femtosecond-UV and femtosecond-NIR pulses over the complete investigated fluence range (1.5–10.5 J/cm^2) and irrespective of the employed YSZ target. For comparison, nanosecond pulses at a wavelength of 193 nm yield only a negligible amount of submicron particles. The particle size distributions in the femtosecond regime are trimodal with maxima around diameters of 80, 150, and 700 nm while the nanosecond pulses yield a unimodal distribution dominated by particles <100 nm in diameter.

The amount of fine particles ejected increases within the first ten pulses as depicted in Fig. 7. Shadowgraphy reveals a simultaneous rise of the shockwave intensity and amount of

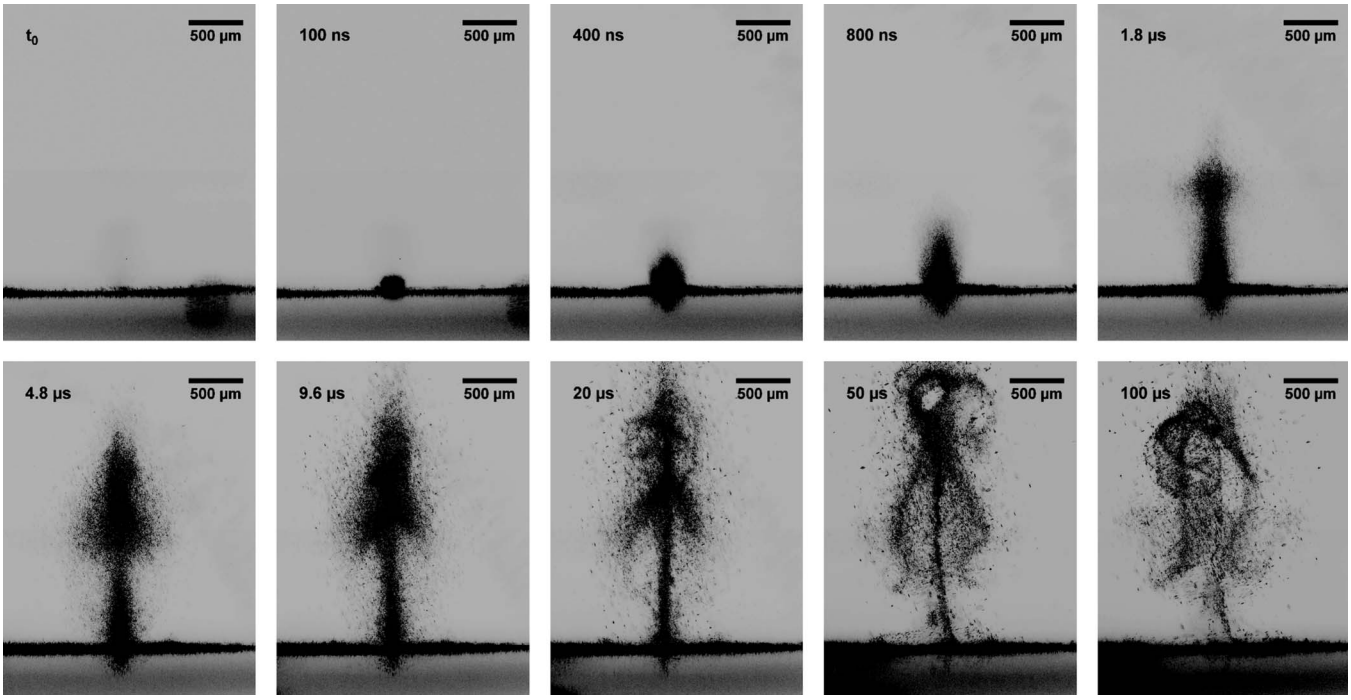

FIG. 5. Time-resolved scattering images visualizing a strong submicron particle ejection from a 9.5YSZ target upon femtosecond-laser ablation (λ: 795 nm, τ_p: 150 fs, 5.5 J/cm^2, and tenth pulse). The same behavior is observed for femtosecond-UV pulses. The images have been inverted for a better representation and comparison to the shadowgraphs shown above.

released material vapor, suggesting that the efficiency of the laser energy coupling to the target material accounts mainly for this phenomenon. As discussed above, this evidences that defect-related incubation contributes to the laser ablation of YSZ even for ultrashort pulses in the NIR. Moreover, a roughening of the surface or an increasing quantity of debris might contribute to an intensified particle ejection.

The time-resolved imaging techniques allow a visualization of particle and fragment expulsion but provide only limited information about their formation mechanism. Scanning electron microscopy (SEM) images depicting the target surface morphology reveal the formation of a dense network of surface cracks by a single pulse even for fluences below the threshold of ablation for all employed lasers and YSZ targets. In the case of a single crystalline target, the cracks are aligned preferentially along the ⟨011⟩ crystallographic direction as shown in Fig. 8. Similarly, oriented cleavage effects have been reported by Constantini *et al.*[37] for YSZ(100) single crystals bombarded with energetic heavy ions.

The damage accumulates with the number of applied pulses, which apparently causes a surface roughening and facile detachment of micron-sized random shaped "tiles" for the fully stabilized 9.5YSZ and 8YSZ targets [Fig. 9(a)]. The partially stabilized 3YSZ target shows a different behavior, revealing only shallow cracks and no indication of severe surface roughening and fragmentation [Fig. 9(b)]. In the case of femtosecond pulses, multipulse exposure yields comparatively rough surfaces, yet not dominated by surface cracking but apparently majorly related to small holelike structures

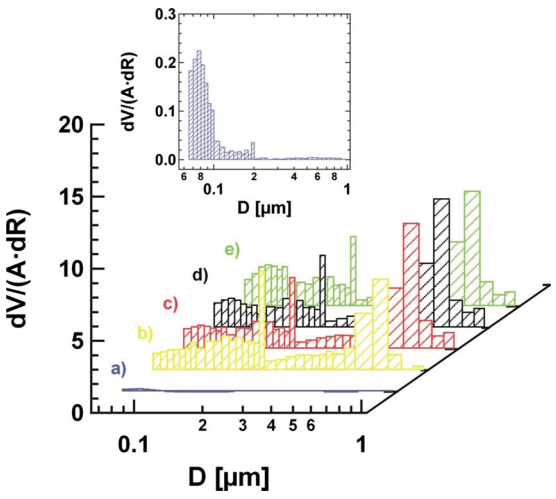

FIG. 6. (Color online) Volumetric aerosol particle size distribution normalized to the laser spot size area A and the spectrometer bin width dR for different YSZ targets and laser sources at a fluence of ~5 J/cm^2: (a) 9.5YSZ (λ: 193 nm and τ_p: 25 ns), (b) 9.5YSZ (λ: 266 nm and τ_p: 150 fs), (c) 9.5YSZ (λ: 795 nm and τ_p: 150 fs), (d) 8YSZ (λ: 795 nm and τ_p: 150 fs), and (e) 3YSZ (λ: 795 nm and τ_p: 150 fs). The inset represents a magnification of (a).

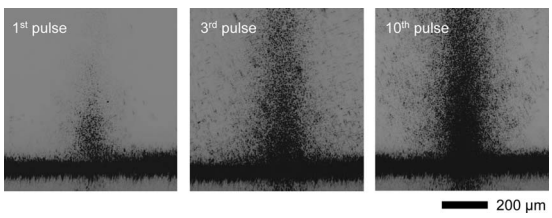

FIG. 7. Scattering images of the volume directly above a 9.5YSZ target taken 4800 ns after the ablating laser pulse (λ: 795 nm, τ_p: 150 fs, and 5.5 J/cm^2) as a function of the number of pulses applied to the same spot. The same behavior is observed for femtosecond-UV pulses. The images have been inverted for a better representation and comparison to the shadowgraphs shown above.

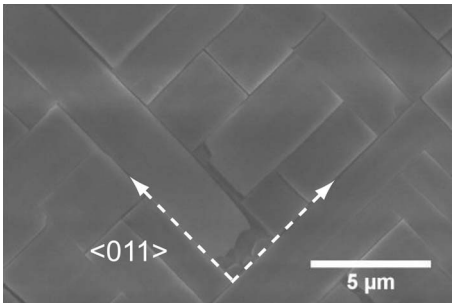

FIG. 8. Surface cracks, preferentially aligned along the ⟨011⟩ crystallographic direction, on a single crystal 9.5YSZ target after single pulse irradiation (λ: 193 nm, τ_p: 25 ns, and 0.8 J/cm^2).

and redeposited submicron spherical droplets, which could be a result of an explosive decomposition via a liquid phase.

Laser-induced cracking of ceramic targets has been observed previously, e.g., on $SrTiO_3$ single crystals[33] or upon microstructuring of YSZ thin films.[24] They originate most probably from the thermomechanical stress generated in the material by the temperature shock caused by the pulsed laser irradiation, which can be estimated according to[14]

$$s = E\alpha(T_m - T_0). \quad (3)$$

The thermomechanical stress is extraordinary large for a material such as YSZ, which combines an extremely high melting temperature T_m with a large elastic modulus E and a large linear thermal expansion coefficient α. It is, e.g., about two orders of magnitude higher than in fused silica, which may account for the observed strong tendency of cracking. The potential of ultrashort pulses to eliminate cracking, demonstrated for $SrTiO_3$,[33] has been assigned to a lower thermal impact on the target as a result of a decoupling of the electron excitation from lattice heating, [44,45] but is not observed for YSZ where femtosecond pulses produce cracks as well. However, as seen above, exfoliation of micron-sized fragments remains restricted to nanosecond-laser irradiation. An explanation could be that in the case of ultrashort pulses, incubation limits cracking to the first pulse(s). The initial low absorptivity is insufficient to cause ablation in this case, which suggests that the deposited energy will be converted entirely to heat.

Figure 10 depicts Raman spectra of a 3YSZ target before and after nanosecond-laser ablation together with a reference spectrum for monoclinic zirconia. The target consists initially predominantly of the tetragonal crystallographic phase revealing six characteristic Raman modes. Minor fractions of the cubic phase, as expected from the phase diagram of the ZrO_2–Y_2O_3 system, cannot be conclusively identified from

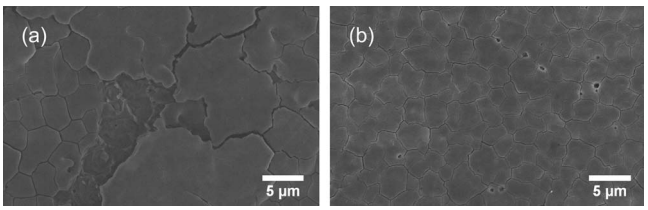

FIG. 9. Surface morphology of (a) an 8YSZ target, and (b) a 3YSZ target after 100 pulses (λ: 193 nm, τ_p: 25 ns, and 1.5 J/cm^2).

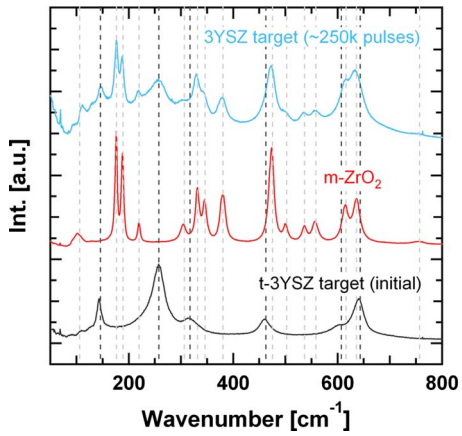

FIG. 10. (Color online) Raman spectra obtained on (a) a sintered 3YSZ target prior to ablation (bottom), (b) ZrO_2 powder as a reference for the monoclinic phase (center), (c) the 3YSZ target after laser ablation with an ArF excimer laser (λ: 193 nm, τ_p: 25 ns, 1.5 J/cm^2, and ~250.000 pulses) (top). The vertical dashed lines mark the peak positions expected for the tetragonal (dark), respectively, monoclinic (light) phase as reported in literature (Refs. 47 and 48).

the Raman spectrum since the strong bands of the tetragonal phase centered around 603 and 640 cm^{-1} overlap in the region ~617 cm^{-1} where the band of the cubic phase is located. After irradiation a phase mixture of the tetragonal and the monoclinic phase is clearly detected. This indicates a laser-induced partial phase transition from the metastable tetragonal to the stable monoclinic phase for 3YSZ. It is well known that this phase transition is essential for the so called transformation toughening process, which accounts for the outstanding mechanical properties of PSZ ceramics. A fissure resulting from a mechanical load may trigger the transformation of a metastable tetragonal grain to the monoclinic phase. This transmutation is accompanied by a significant change in volume by +3%–5% causing a compressive stress field in the matrix around the grain, which counteracts further crack propagation in the material.[2,46] In pulsed laser ablation the transformation may be triggered by the shockwave in the solid, which can easily reach a pressure of several megabars.[45] An analogous process is not possible for the fully stabilized 8YSZ and 9.5YSZ targets, which accordingly exhibit no changes in their Raman spectra that are characteristic for the cubic phase. This difference explains the superior fracture toughness of the partially stabilized 3YSZ ablation target.[47,48]

The superior fracture toughness of PSZ targets allows depositing particle-free YSZ thin films by PLD at moderate fluences (1.2–1.5 J/cm^2) using nanosecond-UV laser pulses [Fig. 11(a)]. At higher fluences an increasing amount of spherical droplets is found in the films [Fig. 11(b)] probably originating from splashing of an extended liquid surface layer formed on the target. Further characterization, e.g., by atomic force microscopy (AFM), x-ray diffraction (XRD), and ion-beam analytical techniques, reveals that the 3YSZ films grown by nanosecond PLD at optimum conditions are dense and smooth with a root mean square roughness of ~4–5 Å and exhibit a chemical composition very close to the respective target. Depending on the substrate temperature, amorphous or crystalline layers can be obtained. The

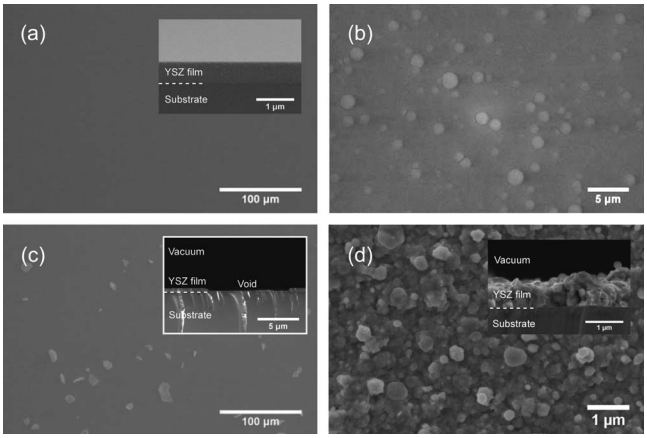

FIG. 11. SEM topview and cross-sectional (insets) images of ~500 nm thick YSZ films deposited by PLD (d: ~40 mm, p_{O_2}: 0.01 mbar, and T: room temperature) for different YSZ targets and laser conditions: (a) 3YSZ (λ: 193 nm, τ_p: 25 ns, and 1.5 J/cm^2), (b) 3YSZ (λ: 193 nm, τ_p: 25 ns, and 3.4 J/cm^2), (c) 8YSZ (λ: 193 nm, τ_p: 25 ns, and 1.5 J/cm^2), and (d) 3YSZ (λ: 795 nm, τ_p: 200 fs, and 1.7 J/cm^2).

particle-free 3YSZ PLD films moreover exhibit a comparable or even enhanced ionic conductivity compared to the state-of-the-art solid electrolyte material, 8YSZ, in the temperature range up to 500 °C rendering them eligible candidates for gas-tight micro-SOFC membranes.[49] Layers grown by ablating a fully stabilized 8YSZ target on the other hand exhibited an incorporation of micron-sized fragments of arbitrary shape irrespective of the laser parameters chosen in the nanosecond regime, which agrees with the ablation studies [Fig. 11(c)]. EDX confirms that the chemical composition of the fragments is identical to the film and target, proving the direct transfer of exfoliated target fragments to the growing film. The inset in Fig. 11(c) depicts a void in the YSZ coating, which is probably caused by the impact and detachment of such a micron-sized fragment.

PLD using femtosecond pulses yields porous and rough (R_q: several 10 nm) layers consisting of agglomerated submicron particles [Fig. 11(d)] irrespective of the employed YSZ target or fluence. This indicates that the strong formation of submicron particles detected by the ablation studies in air for ultrashort laser pulses occurs basically independent of the ambient pressure. The qualitative agreement of the sizes of the particles, which constitute the PLD layers with the aerosol particle size distributions, moreover suggests that a formation or growth by collision-mediated aggregation in the plume[50] is negligible for YSZ. All experimental evidence suggests a direct ejection of the nanoparticles upon laser-target interaction. XRD shows that the films formed by femtosecond PLD are polycrystalline and correspond to the tetragonal, respectively, cubic phase. Higher quality YSZ films by femtosecond-laser ablation may possibly be obtained by more sophisticated approaches, e.g., an optimization by adaptive temporal pulse shaping[51] or multiple pulse arrangements.[22]

IV. CONCLUSIONS

Laser-induced incubative defect formation, which causes residual changes in the target absorptivity, plays an important role not only for nanosecond- but also femtosecond-laser ablation of YSZ enabling efficient material removal also at subbandgap photon energies. The ablation metrics are mainly governed by the laser wavelength while pulse duration, respectively, target microstructure and dopant level have only a minor or no effect.

YSZ is prone to particle ejection in laser ablation, which compromises the quality of PLD-grown films. The intrinsic brittleness of fully stabilized zirconia (8YSZ and 9.5YSZ) inevitably causes severe thermomechanical cracking and an expulsion of micron-sized fragments from the target surface on a microsecond to millisecond time scale for the entire range of laser parameters investigated in the nanosecond regime. The fragments impact on the growing film in PLD, create voids, or are incorporated in the films. Therefore, completely dense and particle-free 8YSZ films cannot be obtained by nanosecond-laser ablation. Partially stabilized 3YSZ withstands the thermomechanical stresses generated by pulsed nanosecond-laser irradiation without exfoliation. Its superior fracture toughness can be attributed to a laser-induced partial transformation of the metastable tetragonal to the stable monoclinic phase. This allows, in contrast to the higher doped fully stabilized YSZ, the growth of particle-free, dense, and smooth 3YSZ films by conventional nanosecond PLD at moderate fluences (1.2–1.5 J/cm^2). Ablation by ultrashort laser pulses prevents the ejection of micron-sized fragments as well but yields a large amount of submicron particles irrespective of the YSZ target and laser wavelength or fluence. Their formation seems to be independent of the ambient pressure and is probably related to a violent phase explosion. Accordingly, PLD using femtosecond-NIR laser radiation yields only rough and porous YSZ layers consisting of agglomerated submicron particles.

ACKNOWLEDGMENTS

The authors gratefully acknowledge the assistance of Ruggero Frison in preparing the ceramic targets and Dr. Razvan Stoian for his technical support on the kilohertz femtosecond laser. They would like to thank Professor Ludwig Gauckler and Dr. Jennifer Rupp for fruitful discussions. The project is part of the program "Nanocrystalline ceramic thin films without sintering" (NANCER) funded by the Competence Center of Material Science and Technologies (CCMX) of the ETH board, Switzerland.

[1] H. G. Scott, J. Mater. Sci. **10**, 1527 (1975).
[2] R. Stevens, *Zirconia and Zirconia Ceramics*, 2nd ed. (Magnesium Elektron Ltd., Leeds, UK, 1986).
[3] D. D. Hass, A. J. Slifka, and H. N. G. Wadley, Acta Mater. **49**, 973 (2001).
[4] A. A. Voevodin, J. J. Hu, T. A. Fitz, and J. S. Zabinski, Surf. Coat. Technol. **146–147**, 351 (2001).
[5] A. P. Caricato, A. Di Cristoforo, M. Fernandez, G. Leggieri, A. Luches, G. Majni, M. Martino, and P. Mengucci, Appl. Surf. Sci. **208–209**, 615 (2003).
[6] P. Mengucci, G. Barucca, A. P. Caricato, A. Di Cristoforo, G. Leggieri, A. Luches, and G. Majnia, Thin Solid Films **478**, 125 (2005).
[7] J. Zhu, T. L. Li, B. Pan, L. Zhou, and Z. G. Liu, J. Phys. D: Appl. Phys. **36**, 389 (2003).
[8] M. S. R. Rao, C. P. D'Souza, P. R. Apte, R. Pinto, L. C. Gupta, S. Srinivas, and A. K. Bhatnagar, J. Appl. Phys. **79**, 940 (1996).
[9] R. Radhakrishnan, A. V. Virkar, S. C. Singhal, G. C. Dunham, and O. A. Marina, Sens. Actuators B **105**, 312 (2005).

[10]A. Bieberle-Hütter, D. Beckel, A. Infortuna, U. P. Muecke, J. L. M. Rupp, L. J. Gauckler, S. Rey-Mermet, P. Muralt, N. R. Bieri, N. Hotz, M. J. Stutz, D. Poulikakos, P. Heeb, P. Müller, A. Bernard, R. Gmür, and T. Hocker, J. Power Sources **177**, 123 (2008).
[11]C. Brahim, A. Ringuede, M. Cassir, M. Putkonen, and L. Niinisto, Appl. Surf. Sci. **253**, 3962 (2007).
[12]H. M. Christen and G. Eres, J. Phys.: Condens. Matter **20**, 16 (2008).
[13]N. Pryds, B. Toftmann, J. B. Bilde-Sorensen, J. Schou, and S. Linderoth, Appl. Surf. Sci. **252**, 4882 (2006).
[14]D. B. Chrisey and G. K. Hubler, *Pulsed Laser Deposition of Thin Films* (Wiley, New York, 1994).
[15]B. Holzapfel, B. Roas, L. Schultz, P. Bauer, and G. Saemannischenko, Appl. Phys. Lett. **61**, 3178 (1992).
[16]K. Kinoshita, H. Ishibashi, and T. Kobayashi, Jpn. J. Appl. Phys. Part 2 **33**, L417 (1994).
[17]A. Marcu, C. Grigoriu, W. H. Jiang, and K. Yatsui, Thin Solid Films **360**, 166 (2000).
[18]T. Kobayashi, H. Akiyoshi, and M. Tachiki, Appl. Surf. Sci. **197–198**, 294 (2002).
[19]E. V. Pechen, A. V. Varlashkin, S. I. Krasnosvobodtsev, B. Brunner, and K. F. Renk, Appl. Phys. Lett. **66**, 2292 (1995).
[20]P. Caminat, E. Valerio, M. Autric, C. Grigorescu, and O. Monnereau, Thin Solid Films **453–454**, 269 (2004).
[21]S. J. Henley, G. M. Fuge, and M. N. R. Ashfold, J. Appl. Phys. **97**, 023304 (2005).
[22]M. Murakami, B. Liu, Z. D. Hu, Z. L. Liu, Y. Uehara, and Y. Che, Appl. Phys. Express **2**, 042501 (2009).
[23]J. Ihlemann, A. Scholl, H. Schmidt, and B. Wolff-Rottke, Appl. Phys. A: Mater. Sci. Process. **60**, 411 (1995).
[24]F. Sánchez, F. Benitez, and M. Varela, Vacuum **65**, 115 (2002).
[25]P. Li, D. Lim, and J. Mazumder, J. Appl. Phys. **92**, 666 (2002).
[26]F. Sanchez, R. Aguiar, P. Serra, M. Varela, and J. L. Morenza, Thin Solid Films **317**, 108 (1998).
[27]A. A. Voevodin, J. G. Jones, and J. S. Zabinski, J. Appl. Phys. **88**, 1088 (2000).
[28]J. Koch, M. Walle, J. Pisonero, and D. Gunther, J. Anal. At. Spectrom. **21**, 932 (2006).
[29]M. Hauer, D. J. Funk, T. Lippert, and A. Wokaun, Opt. Lasers Eng. **43**, 545 (2005).
[30]J. Koch, S. Schlamp, T. Rosgen, D. Fliegel, and D. Gunther, Spectrochim. Acta, Part B **62**, 20 (2007).
[31]T. Lippert and J. T. Dickinson, Chem. Rev. (Washington, D.C.) **103**, 453 (2003).
[32]A. Vogel and V. Venugopalan, Chem. Rev. (Washington, D.C.) **103**, 577 (2003).
[33]S. Zoppel, D. Gray, M. Farsari, R. Merz, G. A. Reider, and C. Fotakis, J. Phys.: Conf. Ser. **59**, 610 (2007).
[34]J. Ihlemann and B. Wolff-Rottke, Appl. Surf. Sci. **106**, 282 (1996).
[35]E. Matthias and Z. L. Wu, Appl. Phys. A: Mater. Sci. Process. **56**, 95 (1993).
[36]V. R. PaiVerneker, A. N. Petelin, F. J. Crowne, and D. C. Nagle, Phys. Rev. B **40**, 8555 (1989).
[37]J. M. Costantini, F. Beuneu, D. Gourier, C. Trautmann, G. Calas, and M. Toulemonde, J. Phys.: Condens. Matter **16**, 3957 (2004).
[38]P. Rudolph, J. Bonse, J. Kruger, and W. Kautek, Appl. Phys. A: Mater. Sci. Process. **69**, S763 (1999).
[39]S. Küper and M. Stuke, Appl. Phys. A: Mater. Sci. Process. **49**, 211 (1989).
[40]S. H. Jeong, R. Greif, and R. E. Russo, Appl. Surf. Sci. **127–129**, 1029 (1998).
[41]L. S. Bennett, T. Lippert, H. Furutani, H. Fukumura, and H. Masuhara, Appl. Phys. A: Mater. Sci. Process. **63**, 327 (1996).
[42]S. H. Jeong, R. Greif, and R. E. Russo, J. Phys. D: Appl. Phys. **32**, 2578 (1999).
[43]Y. B. Zel'dovich and Y. P. Raizer, *Physics of Shock Waves and High-Temperature Hydrodynamic Phenomena* (Dover, Mineola, NY, 2002).
[44]B. N. Chichkov, C. Momma, S. Nolte, F. von Alvensleben, and A. Tunnermann, Appl. Phys. A: Mater. Sci. Process. **63**, 109 (1996).
[45]M. D. Perry, B. C. Stuart, P. S. Banks, M. D. Feit, V. Yanovsky, and A. M. Rubenchik, J. Appl. Phys. **85**, 6803 (1999).
[46]R. H. J. Hannink, P. M. Kelly, and B. C. Muddle, J. Am. Ceram. Soc. **83**, 461 (2000).
[47]E. Fernández López, V. Sánchez Escribano, M. Panizza, M. M. Carnasciali, and G. Busca, J. Mater. Chem. **11**, 1891 (2001).
[48]C. H. Perry, F. Lu, D. W. Liu, and B. Alzyab, J. Raman Spectrosc. **21**, 577 (1990).
[49]S. Heiroth, T. Lippert, A. Wokaun, M. Döbeli, J. L. M. Rupp, B. Scherrer, and L. J. Gauckler, J. Eur. Ceram. Soc. **30**, 489 (2010).
[50]T. E. Itina, K. Gouriet, L. V. Zhigilei, S. Noel, J. Hermann, and M. Sentis, Appl. Surf. Sci. **253**, 7656 (2007).
[51]M. Guillermin, C. Liebig, F. Garrelie, R. Stoian, A. S. Loir, and E. Audouard, Appl. Surf. Sci. **255**, 5163 (2009).